Excitation cross sections for the ns $^2S \rightarrow np$ ^2P resonance transitions in Mg$^+$ ($n=3$) and Zn$^+$ ($n=4$) using electron-energy-loss and merged-beams methods

Steven J. Smith and A. Chutjian
Jet Propulsion Laboratory, California Institute of Technology, Pasadena, California 91109

J. Mitroy
Faculty of Science, Northern Territory University, Casuarina, Australia Northern Territory 0811, Australia

S. S. Tayal
Department of Physics, Clark Atlanta University, Atlanta, Georgia 30314

Ronald J. W. Henry
Department of Physics, Miami University, Oxford, Ohio 45056

K-F. Man
Jet Propulsion Laboratory, California Institute of Technology, Pasadena, California 91109

R. J. Mawhorter
Department of Physics and Astronomy, Pomona College, Claremont, California 91711

I. D. Williams
Department of Pure and Applied Physics, The Queen's University, Belfast BT7 1NN, United Kingdom

Electron-excitation cross sections are reported for the $3s$ $^2S \rightarrow 3p$ $^2P(h,k)$ resonance transition in Mg$^+$ at energies from threshold (4.43 eV) to approximately 9 times threshold (40.0 eV). The electron-energy-loss merged-beams technique used in these measurements is described in detail. In addition, the method of separating contributions of the elastically scattered (Coulomb) and the inelastically scattered electrons in the present Mg$^+$ case and previously reported Zn$^+$ results [Phys. Rev. Lett. **67**, 30 (1991)] is described. Comparisons in the experimental energy range are made for Mg$^+$ with the two five-state close-coupling theoretical calculations carried out herein, and with other published close-coupling, distorted-wave, and semiempirical calculations. The present Mg$^+$ cross sections and Zn$^+$ cross sections from earlier measurements are tabulated.

I. INTRODUCTION

The excitation of singly and multiply charged ions by electron impact plays an important role in understanding heating and radiation mechanisms and electron and ion temperatures and densities in a wide range of high-electron-temperature plasmas [1]. These plasmas comprise such seemingly disparate objects as solar [2] and stellar [3] atmospheres, the interstellar medium [4], planetary ionospheres and magnetospheres [5], and fusion devices [6].

The emission line spectra observed in these high-temperature plasmas can be interpreted to give both energy balance and diagnostics for electron temperature and density. However, as part of the atomic data base needed for such analyses one must have excitation cross sections on the ionic target. The data must cover the threshold region where electron-ion collision cross sections are a maximum [7], where resonance contributions are often significant, and where theoretical calculations are difficult. Given these requirements, and the increasing need for data on both optically allowed and optically forbidden transitions in singly and multiply charged ions, it

was clear that an alternative method was needed to detect directly the inelastically scattered electron in electron-ion collisions. First results of excitation and angular distributions using this energy-loss technique were reported for Zn$^+$ [8], and later extended to Mg$^+$, Zn$^+$, and Cd$^+$, [9,10].

In this paper we report results for excitation of Mg$^+$ ions using a method which resolves many of the drawbacks of the earlier energy-loss measurements. In particular, the present method can be absolute (assuming complete angular collection and absence of overlapping scattering by nearby levels), covers the threshold region by using a merged electron-ion beam geometry to realize an important kinematic effect, and measures (in principle) the entire integral scattering cross section directly, rather than through integration of a differential cross section measured angle by angle. Results for excitation of the resonance transition in Zn$^+$ were presented earlier [11]. Results using a similar technique have been reported for Si^{3+} [12]. We present herein details of the present apparatus, and application to excitation of the resonance transition in Mg$^+$, an astrophysically important ion [13]. We also present cross sections calculated in two five-state

close-coupling theories which differ in their approximation to the target wave functions and in their method of calculating the scattering partial waves.

II. EXPERIMENTAL CONSIDERATIONS

A schematic diagram of the apparatus is shown in Fig. 1. Singly ionized magnesium ions are generated in a discharge ion source [14], without use of a carrier gas. Ions are extracted through a 0.25-mm-diam anode hole by a three-element lens $L1$ and velocity analyzed in a Wien filter. Ions of the appropriate velocity are focused by lenses $L2$ and $L3$ into the center of the merged regions, and then by $L4$ into a deep Faraday cup. Deflector plates D are used to bend the ion beam off axis to prevent either fast, charge-exchanged neutrals or ionizing photons from the ion source from reaching the merged region.

The ion source and Wien filter region are pumped with two oil diffusion pumps. A pumping baffle (tube) B separates the oil-pumped vacuum region from the ultrahigh-vacuum region. The latter is pumped by one ion pump and two cryopumps. Base pressure in the ion source region is 7×10^{-5} Pa, while that of the merged region is 5×10^{-8} Pa. Pressure in the merged region during operation of both beams is 2.7×10^{-7} Pa. Modifications to the beam line have recently been made to replace the Wien filter with a 60° bending magnet to increase the mass resolution in the ion beam and to provide another stage of differential pumping with a second ion pump.

The low-energy electrons are merged with the ion beam in a uniform, stable solenoidal magnetic field through the use of trochoidal ($\mathcal{E} \times \mathcal{B}$ fields) deflection plates (MP's) [12,15]. Inelastically scattered electrons from the merged, interaction region are demerged by a second set of analyzing trochoidal plates (AP's) which disperse the electrons according to their final longitudinal and radial velocities. (We point out that a similar experimental geometry has been used in Ref. [12] to carry out excitation measurements in Si^{3+}. Differences between the two approaches are noted below.) In order to reduce background contributions from the intense parent electron beam, that beam is trochoidally deflected by plates DP out of the plane defined by the directions of $\mathcal{B}$ and $\mathcal{E} \times \mathcal{B}$ and trapped in a deep Faraday cup. The density profiles in both beams are measured simultaneously using

four separate vanes with radially spaced holes which take "slices" through the beams (see details below). The entire experiment is mounted on a 15-mm-thick titanium plate whose faces have been ground flat and parallel to 0.1 mm. The plate can be removed from the magnet bore along titanium rods mounted within the bore.

The inelastically scattered electrons are measured using a position-sensitive detector (PSD). The PSD is a 40-mm-diam microchannel-plate array with a resistive anode. The front face is oriented normal to the direction of $\mathcal{B}$ and masked by a titanium plate to a rectangular viewing area. Two sets of highly transmitting grids are used to carry out retarding-potential measurements on the scattered electrons. The entire unit is housed in a titanium can for shielding purposes. The four separate corner signal leads from the resistive anode exit the vacuum chamber and enter a four-channel preamplifier.

A block diagram of the electronics is shown in Fig. 2. Control is through a computer-aided measurement-and-control (CAMAC) crate and an IBM/AT personal computer (PC). Briefly, the four phases of electron counts detected at the PSD resistive anode is routed into two sections of a histogramming memory, depending on the cycle of the beams chopping unit. The time spent in each cycle is clocked through a 10-MHz clock and quad scaler. These times are stored in the PC and later used to convert signal counts into signal rates. A typical experimental run consists of about 500 sec of data accumulation. Each run is preceded or followed by a measurement of the beam profiles to establish the overlap integral. These profiles are measured with a microstep motor controlled by a countdown timer portion of a scaler-timer in the CAMAC crate. The scaler-timer commands the PC to drive the microstep motor with pulses from the PC's communication port. Separate charge-pump digitizers convert the analog electron and ion currents (from the respective Faraday cups) into digital pulses which the scaler-timer also counts. After a preset counting signal, a start command is sent to the PC, along with the stored digitized currents transmitted through the beam profile vanes. Each command to advance to a new vane position is followed by a 0.2-sec "pause" which gives both beams an opportunity to "settle." This is followed by a 1–5-sec counting period (depending upon the beams currents). These counts are then transferred to the PC, and a new
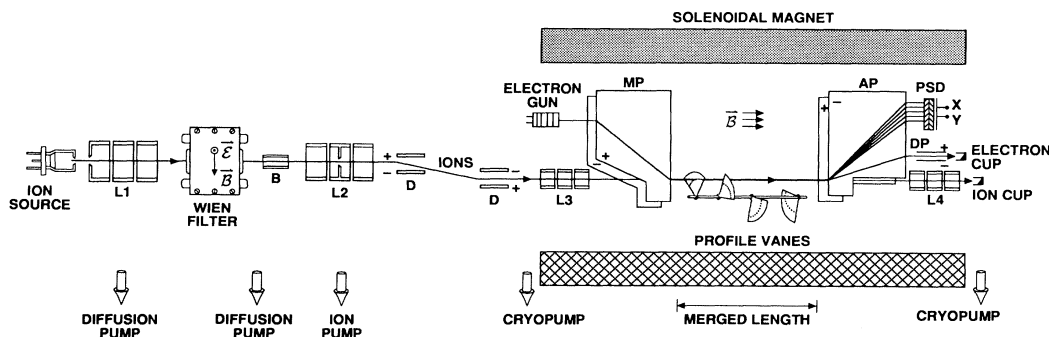

FIG. 1. Experimental setup: ($L1-L4$) three-element focusing lenses, (B) differential pumping baffle, (D) deflector plates, (MP) merging trochoidal plates, (AP) electron analyzing trochoidal plates, (DP) trochoidal deflection plates to deflect parent electron beam out of the scattering plane, (PSD) position-sensitive detector.
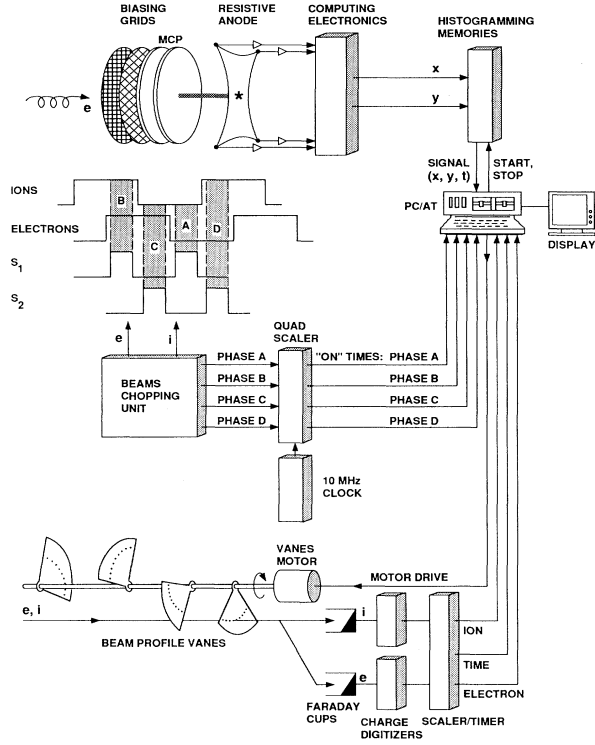
FIG. 2. Schematic block diagram of instrument controls. The following units are located in a CAMAC crate: quad scaler, 10-MHz clock, charge digitizers (2), scaler-timer, histogramming memories (2), and (not shown) a DAC and an ADC.

vane position commanded. A complete profiles measurement takes about 10–12 min.

The energy-loss approach. In this technique one detects directly, in an electron-ion collision, the inelastically scattered electron. For an ion A^{m+} of charge $m+$, initial state nl and final state $n'l'$, the process is given by

$$e(E_e, 0°) + A^{m+}(nl, E_i) \rightarrow A^{m+}(n'l', E_i - \Delta E_i)$$

$$+ e(E_e - \Delta E_e, \vartheta) . \qquad (1)$$

Here, the incident electron e and ion A^{m+} have laboratory energies E_e and E_i, respectively. The inelastically scattered electron has energy $E_e - \Delta E_e$ and laboratory scattering angle ϑ relative to the incident electron beam ($\vartheta = 0°$). The detected particle is the electron $e(E_e - \Delta E_e, \vartheta)$. By virtue of its spin and charge, the electron is able to excite both optically allowed and optically forbidden transitions in $A^{m+}(nl)$. This approach was introduced from electron-neutral scattering [16] into the area of electron-ion collisions [8].

The center-of-mass (c.m.) energy is obtained from the individual laboratory energies, masses, and angle between the two beams [see Eq. (5) below]. The inelastic energy $\Delta E_{c.m.}$ absorbed during the collision, expressed in the c.m. frame ($\Delta E_{c.m.} = 4.43$ eV) is carried away by both the electron and ion. The outgoing laboratory energies for the electron and ion are $E_e - \Delta E_e$ and $E_i - \Delta E_i$, respec-

tively, and vary with the final c.m. scattering angle due to momentum conservation. Expressions for the energy sharing are [17]

$$\Delta E_e = \frac{\mu}{m_e} \Delta E_{c.m.} + \mu v f \left\{ \cos\theta \left[1 + \frac{\Delta E_{c.m.}}{E} \right]^{1/2} - 1 \right\} ,$$

$$\qquad (2a)$$

$$\Delta E_i = \frac{\mu}{m_i} \Delta E_{c.m.} + \mu v f \left\{ \cos\theta \left[1 + \frac{\Delta E_{c.m.}}{E} \right]^{1/2} - 1 \right\} ,$$

$$\qquad (2b)$$

where $\mu = m_e m_i / (m_e + m_i)$ is the reduced mass, f the velocity of the c.m., θ the c.m. scattering angle, E the c.m. energy, and v the relative laboratory velocity of the incident particles. The fact that the c.m. velocity and ion laboratory velocity are parallel has been used in Eq. (2). One also notes that an electron and ion can undergo energy loss in the laboratory frame even for the case of elastic scattering ($\Delta E_{c.m.} = 0$).

The merged electron- and ion-beams technique. The use of merged beams, rather than the crossed beams used in earlier work, was dictated by the need to (a) have a greater collision volume, so that signal rates would be higher, and (b) realize a small kinematic advantage that would allow one to carry out measurements at threshold in the c.m. frame, but yet detect electrons having energies of 0.1–0.2 eV in the laboratory frame (see below).

In merged-beams geometries the faster beam (electrons, in this case) is continuously overtaking the slower (ion) beam: the electrons are playing "catch-up" on the ions. As a result the distance over which the beams interact is slightly shorter than the merged geometric path-length L_0. To account for this, one notes that the time the beams spend in the interaction region is L_0/v_e. In this time the ion beam travels a distance $(L_0 - L')/v_i = L_0/v_e$, so that the merged length corrected for catch-up is [15]

$$L' = L_0 (1 - v_i / v_e) , \qquad (3)$$

where v_e and v_i are the electron and ion velocities (cm/sec), respectively. For a 5.50-eV electron and a 4-keV Mg^+ beam, the worst-case foreshortening is $L'/L_0 = 0.872$.

Another effect is that the electron path length is made slightly larger than geometric due to spiraling of the electrons in the solenoidal field. This spiraling arises from a small component of electron velocity perpendicular to $\mathscr{B}$, and the effect is to increase the path length to an amount L given by [18]

$$L = L_0 (1 + 0.5 E_\perp / E) = L_0 (1 + \sin^2\alpha) , \qquad (4)$$

where $E_\perp$ is the electron kinetic energy perpendicular to $\mathscr{B}$, and α is the electron pitch angle. For $\alpha = 5°$ [19] one has $L/L_0 = 1.0076$.

The absolute excitation cross section $\sigma(E)$ at the c.m. energy E is related to the experimental parameters by

$$\sigma(E) = \frac{Re^2F}{\epsilon I_i I_e L}\left|\frac{v_e v_i}{v_e - v_i}\right|, \qquad (5)$$

where R is the total signal rate (sec^{-1}), e the electron charge, I_e and I_i the electron and ion currents (A), respectively, L the merged pathlength (cm) corrected for spiraling [Eq. (4)], ϵ the intrinsic detection efficiency of the PSD, and F the overlap factor between the electron and ion beams (cm^2). The rate R corresponds to that for an instrumental collection geometry which accepts the entire $\{0, \pi\}$ c.m. angular range [braces $\{\ \}$ denote intervals]. Since there is not complete collection, near threshold, at the present relatively low ion energies, one measures herein a reduced rate R', and applies a correction from theory ("forward to back") to account for the uncollected, backward scattering (see Sec. IV and Tables VIII and IX). Finally, since only the magnitude of the relative velocity in Eq. (5) is relevant to the scattering, the same c.m. energy can be obtained with different combinations of electron and ion velocities. This serves as a useful diagnostic of the final cross section, which must be independent of the chosen combination. Typical operating parameters are listed in Table I.

One has an important center-of-mass effect exploited in the present work. Because of the "catch-up" noted above, the c.m. collision energy is slightly reduced over the laboratory energy of the electrons. To see this, one uses the energy transformation given by [20]

$$E = \mu\left[\frac{E_i}{m_i} + \frac{E_e}{m_e} - 2\left[\frac{E_i E_e}{m_i m_e}\right]^{1/2}\cos\psi\right]$$

$$= E^+ + E_e - 2(E^+ E_e)^{1/2}\cos\psi \quad (m_e \ll m_i), \qquad (6)$$

where E^+ is the reduced ion energy given by $E^+ = (m_e/m_i)E_i$, and ψ is the angle between the two beams (taken as $\psi = 0°$ for merged beams). For a 4.0-keV ion beam, $E^+ = 0.0904$ eV corresponding to a mixture

TABLE I. Typical operating parameters and backgrounds for the energy-loss merged-beams apparatus.

Parameter	Value
Electron current I_e	0.15 nA
Ion current I_i	20 nA
Merged geometric path length L_0	20.0 cm
Beam overlap factor F	$(5-17)\times 10^{-3}$ cm^2
Electron beam diameter	0.12 cm
Ion beam diameter	0.22 cm
Energy resolution (FWHM)	0.35 eV
$|\mathcal{E}|$ (in MP)[a]	32 V/cm
$|\mathcal{E}|$ (in AP)[a]	22 V/cm
Electron background B_e	8 kHz
Ion background B_i	4 KHz
Electronic noise B_n	100 Hz
Signal rate R	5–50 Hz
Dead-time correction	5%

[a]For 10-eV electrons.

89% ^{24}Mg$^+$ and 11% ^{25}Mg$^+$ in the beam, corrected for nuclear binding. For excitation near threshold, say $E - \Delta E_{\text{c.m.}} \sim 0.1$ eV, the residual energy of the outgoing electron can be calculated to be 0.15–0.30 eV, depending on the c.m. scattering angle [17]. And hence, one may excite the Mg$^+$ $3s \to 3p$ transition near threshold, while having a 0.15–0.30-eV energy (laboratory frame) electrons. This also implies that one may orient the PSD perpendicular to $\mathcal{B}$ and still detect threshold electrons; and at any distance from the end of the analyzing plates, since the electrons are locked onto $\mathcal{B}$. A different geometry was used in Ref. [12], where the PSD was oriented parallel to $\mathcal{B}$. This necessitated "clamping" the trochoidal field right up to the point of final acceleration of the electrons onto the front microchannel-plate surface. In effect, the PSD in Ref. [12] was immersed in the field of the trochoidal plates.

In addition to the energy transformation of Eq. (6), there is a transformation between the laboratory (ϑ) and c.m. (θ) scattering angles which can be shown to be given by

$$\tan\vartheta = \frac{\sin\theta}{\cos\theta + \rho}, \qquad (7a)$$

where

$$\rho = \frac{\left[\dfrac{E^+}{E_e}\right]^{1/2} + \dfrac{m_e}{m_i}}{\left\{1 + \dfrac{E^+}{E_e} - 2\left[\dfrac{E^+}{E_e}\right]^{1/2} - \dfrac{\Delta E_{\text{c.m.}}(m_i + m_e)}{m_i E_e}\right\}^{1/2}}. \qquad (7b)$$

The trochoidal plates. The use of trochoidal deflection to carry out energy-loss analysis of scattered electrons is a relatively new technique exploited herein, and is also used by Cloutier and Sanche [21], and Wåhlin *et al.* [12]. Extensive characterizations of the trochoidal trajectories exist [21–24], and the reader is referred to these studies for further details.

The elements of trochoidal deflection relevant to the present work are the deflection of the electron beam as a function of residual energy and the so-called "beam shear." The deflection of the electron beam results from the vector addition of the beam's axial velocity and the drift velocity $\mathbf{v}_D$ of the trochoidal deflector given by $\mathbf{v}_D = \mathcal{E} \times \mathcal{B}/|\mathcal{B}|^2$ (m/sec). Further details of the electron motion will depend upon fringing electric fields, the projection of the electron energy in the axial direction, and on the starting laboratory polar (ϑ) and azimuthal (φ) angles of the electron trajectory.

The resulting motion is complicated by the fact that, given a nonzero diameter of the electron beam, not all portions of the beam experience the same deflection within the trochoidal plates. That part of the electron beam closer to the positive electrode will be accelerated upon entering the electric field of the plates, while that closer to the negative electrode will be decelerated. The accelerated portion, after vector coupling to $\mathbf{v}_D$, will be deflected less than the decelerated portion. A round beam at the plate entrance will be deflected and elongated

into an elliptical shape at the exit. A measure of the tilt of the beam cross section with respect to the electric-field direction is the "shear angle" γ given by

$$\tan\gamma = \eta d^3 \mathcal{B}^2 / \mathcal{E} D^2 \, , \qquad (8)$$

where $\eta = e/m$, d is the deflected distance, and D is the length of the plates [25]. Given the effects of deflection, beam shear, and fringing of the electric field at the entrance and exit, all calculations of the shape ("footprint") of the final electron image on the PSD were carried out with the SIMION charged-particle computer code [26] for beams with no space-charge loading, and for the geometry of our apparatus.

Beams profile measurement. The measurement of the form factor F in Eq. (5) is carried out by the use of a slotted-vane system [27]. In this approach, four molybdenum beam-scanning segments are mounted on a shaft driven by a microstep motor located outside the vacuum system. Each segment contains nine pinhole apertures evenly spaced at increasing radial distances (6.73–7.24 cm) from the center of rotation. As the shaft rotates, the holes travel across the merged beams, and each hole sweeps through a different portion of the beams. The electron and ion currents transmitted through the apertures are collected in their separate Faraday cups, and their levels are recorded with a charge-pump digitizer along with information on the hole position as read from an encoder. Calibration of shaft position with hole location was calculated from the geometry. It was then measured with a theodolite and checked by launching a laser beam along the merged length and visually recording maxima in the transmitted light intensity.

The diameter of each aperture was 0.3 mm. For the smaller (electron) beam diameter of 1.0 mm (average) this gives a ratio of hole area to beam area of 0.09. The form factor F in (cm^2) is the two-dimensional overlap as measured at each of the four segment locations. It can be written as

$$F = \frac{\int\int I_e(x,y,z_k)dx\,dy \int\int I_i(x,y,z_k)dx\,dy}{\int\int I_e(x,y,z_k)I_i(x,y,z_k)dx\,dy} \qquad (9)$$

for each segment location z_k $(k=1\text{--}4)$.

Double-beams modulation. There are a number of sources of backgrounds in electron-ion collisions experiments. Backgrounds arise from ionizing collisions of the ion beam with surfaces and the residual gas (B_i), collisions of electrons with surfaces and residual gas (B_e), and electronic noise from the PSD and associated preamplifier and electronics (B_n). The actual signal (S) can be orders of magnitude smaller than the sum of backgrounds (Table I). In order to eliminate B_i, B_e, and B_n, a double-beams modulation technique was used, similar to that of Molyneux, Dolder, and Peart [28] and by Havener et al. [29]. In the present work, the modulation scheme allowed for the following: (a) a variable chopping period, (b) variable "on" widths of the counting scalers, (c) built-in logic delays (variable) which gated the scalers "off" 25 μsec prior to a change of state of either the electron or

ion beams, (d) a 180° change of phase every 2^6 ion pulses, and (e) a variable delay of the ion gating pulse relative to the electron gate to allow for the flight time ($\sim$12 μsec) between the point of ion deflection and the center of the merged collision region. The use of (c) permits both beams to settle after being turned on and prevents any sharp transients during changes of state from being counted. With (d), one averages the signal counting between the leading and trailing portions of the beams. The chopping frequency was varied in the range 0.4–2.0 kHz, and no systematic effects on cross section were observed. The frequency used in these measurements was 1 kHz, corresponding to a time constant of 1 msec, as opposed to a time constant of the vacuum system estimated to be 35 msec.

The four phases of modulation and gating of scalers S_1 and S_2 are indicated in Fig. 2. The meaning in the sequence is as follows: [A] electron beam "off", ion beam "off", and S_1 counts B_n; [B] both electron and ion beams "on", and S_1 counts $S + B_e + B_i + B_n$; [C] electron beam "on", ion beam "off", and S_2 counts $B_e + B_n$; [D] electron beam "off", ion beam "on", and S_2 counts $B_i + B_n$. The net signal S is given by the difference in accumulated counts in scalers S_1 and S_2. Typical electron count rates on the PSD during each of the four phases are [A] < 0.5 kHz, [B] 25 kHz, [C] 16 kHz, and [D] 8 kHz.

Detector assembly. The detector assembly consists of two rectangular, 92% (nominal) transmitting woven tungsten grids placed in front of the PSD. A schematic diagram of the assembly is shown in Fig. 3. The PSD is a commercially available unit made up of two 5.1-cm-diam microchannel plates (MCP's) and a resistive-anode (RA) array. The entire assembly is housed in a titanium can to shield the MCP's against stray electrons and to shield the merged region from high voltages on the MCP's and the RA. Dimensions of the titanium can are 8.9 cm
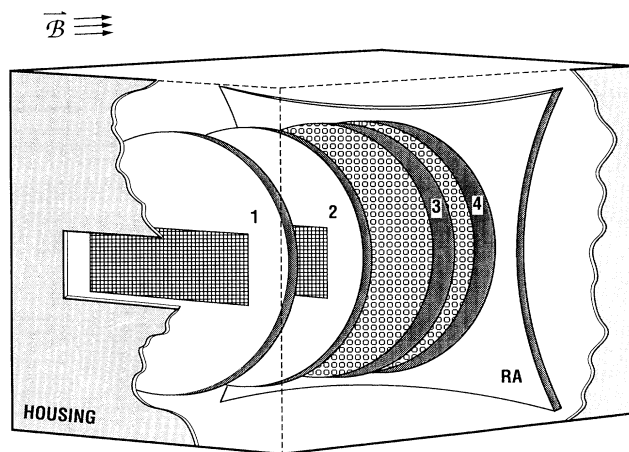

FIG. 3. Schematic diagram of the detector assembly. Electrons spiraling along $\mathcal{B}$ enter the titanium housing from the left through the rectangular aperture. The elements are the following: 1,2, gridded apertures; 3,4, microchannel plates; RA, resistive anode.

(length)×7.5 cm (width)×7.5 cm (height). A rectangular slot on the can (ungridded, dimensions 1.3×4.1 cm) defines the viewing area of the MCP's. Gridded slots of the same dimension are placed at positions 1 and 2. All mounting plates are made of commercially pure titanium and insulated spacers of machinable ceramic.

The spacings 2-1 and 3-2 are 0.6 and 0.4 cm, respectively. The spacing 4-3 is approximately 0.01 cm, and RA-4 is 0.2 cm. Both are set by the manufacturer. Grid 1 is recessed approximately 2.5 cm from the opening on the housing. Nominal voltages on the various elements are the following: housing (grounded), grid 1 (grounded), grid 2 (variable, 0.0− −50 V depending on the scattered electron energy), MCP 3 (front at +850 V, rear at +1600 V), MCP 4 (front at +1600 V, rear at +2300 V), and RA (+2500 V).

Electron-energy-scale calibration. The electron energy scale was calibrated by observing the onset of the $3s \rightarrow 3p$ transition. A downward shift of 1.0 V (with uncertainty 0.1 V) was applied to the nominal cathode voltage to obtain the true electron energy needed to generate the onset at 4.43-eV c.m. energy. The shape of the onset will be due to convolution of the rapid, finite onset with the electron energy width (estimated to be 0.35 eV). The 1.0-eV calibration offset accounts for the contact potentials of the system. This includes contributions from the gun cathode (BaO-impregnated porous tungsten), merging and analyzing plates (titanium), the table below the collision region (titanium), and grids (tungsten) within the MCP housing (titanium). It is reasonable to expect that the largest contribution to the contact potential is through the low work-function cathode, and that the contact potential between the final grid wires (tungsten) and the collision region (titanium) will be, in principle, less than or equal to the difference in work functions 4.55(W)−4.33(Ti)=0.22 eV [30]. An electron would require this (laboratory) energy to enter the retarding grids under the "low-retard" (nominal voltage $G_2 = 0$). This poses no problem, since the inelastically scattered electron, even for results near threshold, still has at least 0.22-eV laboratory energy for scattering angles $\vartheta < 90°$. It is known through trajectory calculations that the plates AP can direct electrons of laboratory energy 0.1–0.2 eV onto the MCP.

Detector calibration. Calibration of the absolute detection efficiency of the PSD was made using techniques similar to those described elsewhere [31,32]. Measurements were made with the two 92%-transmitting grids in place, so that the results reported refer to the combined effects of the grids and the PSD efficiency. Referring to Fig. 1, the magnetically collimated electron beam could be directed either into the Faraday cup or onto the PSD. Currents in the Faraday cup were measured with a direct-reading metal-oxide-semiconductor field-effect-transistor (MOSFET) based electrometer capable of reading currents to less than 10^{-16} A. Currents on the PSD were read as the transistor-transistor-logic (TTL) rate signal from the computing electronics, signifying a valid x,y event on the PSD which exceeded a preset threshold. A comparison between the current and rate then gives the absolute detection efficiency of the PSD plus grids. This

total efficiency was found to be $\epsilon = 0.836 \pm 0.011$. It includes secondary electrons generated at grid 2 and accelerated to the MCP 3 surface, and secondary electrons produced at the MCP 3 surface and repelled back to MCP 3. Effects of a changing secondary-electron emission coefficient with energy (range 0–50 eV, and tungsten grid wires [33]), and changing MCP detector efficiency with energy (range 850–900 eV [32]) were calculated to be at the 0.8% and 0.5% levels, respectively, and were considered negligible. The measured value of ϵ is also seen to be smaller than, as expected, the 92% transmission of two perfectly aligned grids.

Dead time. There is a nonzero time required for an individual microchannel on the PSD microchannel plate to cascade amplify an impinging electron. This time is limited by the bias ("strip") current of the MCP. There is also a nonzero time required for the subsequent computing electronics to register the (x,y) location of that event, amidst other events occurring "simultaneously" on the MCP. Any subsequent pulses requiring position processing within this computing time are essentially lost to the experiment. The total PSD electronics dead time is composed of two elements, one of which is paralyzable (the pulse pileup rejector in the preamplification stage), and the other nonparalyzable (the eight-bit analog-to-digital converter) [34]. To avoid large dead-time losses, or to keep required corrections small, the counting rate both within each microchannel, and over the unmasked area of the MCP (Fig. 3), must be kept low.

In the present case, the count rate over the portion of the MCP outside the rectangular viewing area is negligible (<0.1 kHz) and does not contribute to dead-time losses. Moreover, bias ("strip") current effects are also negligible. As stated by the manufacturer [35], the pair of MCP's in use is capable of supporting count rates of approximately 50 electrons/microchannel sec. Rates in the present work are much less than this due to the spatially broad nature of the backgrounds and signal, and are estimated to be of the order of 0.1 electron/microchannel sec. Furthermore, such effects would reveal themselves in nonlinearities of scattered signal with I_e and I_i. No such nonlinearities were detected in measurements on Zn^+, Mg^+, and O^+ under conditions where the product of I_e and I_i was varied over a factor of 25.

The principal source of dead time lies in the rate of electrons incident on the MCP relative to the limiting rate at which the PSD computer can process each electron "hit" to an (x,y) location. This dead time was measured in the present work by directing a weak, diffuse electron beam ($10^{-14} - 10^{-16}$ A) onto the PSD. By counting the rate output (the response to all normal gain events up to about 1 MHz) relative to the strobe output (response to only events accepted for x,y processing) the dead-time efficiency was determined in the range 1.0–200 kHz. Correction factors were 1.01 at a rate of 20 kHz, 1.04 at 30 kHz, and 1.09 at 40 kHz. There was also agreement over the larger rate range, at the 5% level, with the manufacturer-provided dead-time curve for the eight-bit ADC [35].

In order to avoid large (or any) dead-time corrections,

it was decided to use low currents of ions and electrons. The maximum rate was always less than 30 kHz, and was usually in the range 10–20 kHz. This placed count rates comfortably below the region where corrections of more than 5% would be required. Advantage was also taken of the fact that the ion, electron, and electronic noise backgrounds were dispersed on the MCP, while the signal (and its superimposed backgrounds) was confined to a much smaller region. This was apparent by viewing the extent of the signal and background regions on the MCP.

A problem which arises is that the PSD has to process widely varying count rates during the beam-modulation phases $[A]$, $[B]$, $[C]$, and $[D]$, with very low rates present in $[A]$ and higher, different rates in $[B]$, $[C]$, and $[D]$. One solution [12] to this "differential dead-time" problem is to route the counts in phases $[A]$–$[D]$ to different memories, calculate count rates, apply dead-time corrections to each phase, then calculate the corrected signal rate from $\dot{S} = [\dot{A}]_c + [\dot{B}]_c - [\dot{C}]_c - [\dot{D}]_c$ [the notation refers to corrected (c) rates $(\cdot)$]. Another method, appropriate at lower count rates (less than approximately 20 kHz, where dead times are small), was used herein. The signal counts are processed in hardware, in real time, by $S = [A] + [B] - [C] - [D]$. The resulting signal S is stored, then converted to a rate $\dot{S}$ by dividing by the total elapsed time in the phases. The dead-time correction is applied by noting the count rates in each phase on the PSD rate meter. In most cases, this dead time is dominated by counting rates during phases $[B]$ and/or $[D]$ (which are, again, less than about 20 kHz). The average counting rate is $\langle R_{\text{rate}} \rangle = \{[\dot{A}] + [\dot{B}] + [\dot{C}] + [\dot{D}]\}/4$.

Relative to the backgrounds, the signal is generally localized to a smaller fractional area of the MCP than are the more diffuse backgrounds. One may use this to advantage in that the signal S can be totally contained within that area, but only the included fractional area of the backgrounds is counted (examples of the signal's spatial extent are given in Fig. 5). Under the present experimental conditions, the dominant backgrounds occur in phases $[B]$ and $[D]$. It was found that simply doubling the rate to $2\langle R_{\text{rate}} \rangle$ to account for the duty cycle in these two phases could determine the dead-time correction to be applied to $\dot{S}$. The signal rate $\dot{S}$ is corrected upward by a factor determined by the electronic dead-time curve supplied by the manufacturer and checked herein. The typical dead-time correction is 5%, and a maximum 25%. The error incurred in calculating $\dot{S}$ by this method, relative to that incurred by separate binning of the phases $[A]$–$[D]$ then correction of the individual rates [12], is calculated to be less than 2% over the range of backgrounds encountered herein. Moreover, the correction tends to underestimate the true signal rate, since $2\langle R_{\text{rate}} \rangle$ must be less than the largest rate in any phase (which incurs a slightly larger correction). The error in this correction is thus a one-sided uncertainty $^{+2}_{-0}\%$, which is added linearly to the quadrature combination of other uncertainties (see Sec. IV and Table VII).

The overlap between elastically and inelastically scattered electrons. The trochoidal plates deflect an electron by coupling the drift velocity v_D to the axial velocity of the electrons. A problem that arises is that an elastically scattered electron at a laboratory angle ϑ can have the same axial velocity as an inelastically scattered electron at a smaller ϑ, and hence these two electrons would occupy the same position on the PSD. Because the elastic scattering can have a larger differential cross section (DCS), this competition can mask the inelastic signal to some extent, depending on ϑ (and, for multiply charged ions, on the ion charge Z_i, since the elastic DCS scales as Z_i^2). It gives rise to a background inherent to the collision, and one that cannot be eliminated by double-beams modulation. The critical laboratory angle ϑ_c above which interference can occur is given in terms of the laboratory energies by

$$(E_e - \Delta E_e^{\text{el}}) \cos^2 \vartheta_c = (E_e - \Delta E_e^{\text{inel}}) , \qquad (10)$$

where ΔE_e^{inel} is evaluated from Eq. (2a) at $\theta = 0°$ and $\Delta E_{\text{c.m.}} = 4.43$ eV; and ΔE_e^{el} at $\theta = \theta_c$ and $\Delta E_{\text{c.m.}} = 0.0$ eV. The values of θ_c and ϑ_c are related through Eqs. (7a) and (7b). For the example of Mg^+ excited near threshold, one has $E_e = 5.87$ eV, $\Delta E_e^{\text{el}} = 1.19$ eV, $\Delta E_e^{\text{inel}} = 5.54$ eV $(\theta = 0°)$, and $\vartheta_c = 74.6°$.

Extensive modeling of the overlap has been carried out both on the previous measurements in Zn^+ and on the present Mg^+ results. The underlying philosophy of this modeling is to provide a parallel, theoretical path to the experimental technique of subtracting the elastic contribution from the inelastic signal. *The modeling provides a framework to illustrate within the present, specific experimental geometry how the inelastic signal can dominate over the elastic signal.* As such, assumptions in the modeling do not contribute to experimental errors. Discrimination between elastic and inelastic scattering is realized *experimentally* by (a) the energy dispersion of the analyzing plates (AP's), (b) use of the retarding grids, (c) the choice of baseline from visual inspection of the inelastic spectrum, and (d) setting of the "region of interest" (ROI) on the PSD. In (d), the inelastically scattered electron footprint is centered in the ROI. The ROI is chosen using two methods: first, the SIMION code is used to calculate where the footprint should be, and second, a low-current electron beam of the desired residual energy is deflected onto the PSD and observed to lie in the center of the ROI.

Two methods of baseline subtraction were applied. In the first method, used earlier for Zn^+, a minimum counts threshold was established through visual determination of where the signal blends into the background. Counts below this threshold were truncated during data reduction. In the second method, used for Mg^+, the baseline is successively raised until an incremental increase results in a total excluded count which exceeds the value expected from elastic scattering. This estimate is then compared to a visual estimate of the baseline. Both methods are described in detail in the following.

A. Method I: Footprint analysis for Zn^+

Data collected by the PSD during the actual experiment is stored in a 256×98 array. After data accumula-

tion and during analysis, one visually selects from the experimental spectrum the x_{start}, x_{stop}, y_{start}, and y_{stop} counting region, as well as the minimum count threshold n_{min}. If the signal is below a certain n_{min} then a zero is assigned to that particular pixel during data reduction. The region-of-interest parameters x_{start}, x_{stop}, y_{start}, and y_{stop}, as well as the counts threshold n_{min}, are chosen solely from the experimental spectrum.

In a parallel effort, and as a check of the experimental choice of the ROI parameters, the expected footprints of both elastic and inelastic scattering on the PSD were modeled. This was done for the present instrument geometry (plate lengths, gaps and locations, and detector location; electric and magnetic fields) using the SIMION trajectory-simulation code. The code neglects space charge, deemed reasonable for the low currents of electron and ion beams (and their sum) encountered here. For comparison between experiment and model footprints, the case of $E_e = 39.8$ eV primary electrons ($E = 37.5$ eV) results in inelastically scattered electrons with 33.5-eV laboratory energy for $\theta = 0°$ [for other θ see Eq. (2a)]. At this energy the inelastic cross section is known, from theory [36], to be forward peaked, with most of scattering occurring at angles less than $\theta = 40°$. By using the retarding grids one limits the elastically scattered electrons to only those which scatter through more than $\vartheta_c = 22.9°$. The experimental parameters are $|\mathscr{B}| = 42$ G and $|\mathscr{E}| = 63$ V/cm. The beam diameter was taken to be 1 mm (full width at base), as observed experimentally. The SIMION code was used to launch both inelastic and elastic electrons displaced in 0.25-mm steps over the interval $\{-0.5, 0.5$ mm$\}$ about the beam center to account for beam shear. For the inelastic electrons the polar angle ϑ was varied from 0° to 40°. For elastically scattered electrons ϑ was varied from 22.9° to 60°. Of importance is the variation in azimuthal angle φ, which for the larger angles ϑ caused the elastic footprint to spread out considerably, and was varied over the full range $\{0, 2\pi\}$ for each ϑ. SIMION allows three-dimensional (3D) projection of all trajectories, and successive plots were made using the full range of (ϑ, φ) launch angles at each electron-beam displacement. A total of 105 trajectories were computed for Zn^+. The model footprint size was calculated for each case. For the elastic electrons the Coulomb formula was used to determine the elastic cross section between a given ϑ and $\vartheta + d\vartheta$. The elastic scattering can be calculated from the Coulomb formula (in Gaussian units) [37]

$$\frac{d\sigma_{el}}{d\Omega} = \left[\frac{Z_i e^2}{4E \sin^2(\theta/2)} \right]^2, \tag{11}$$

which reduces to (for $Z_i = 1$, and E in eV) $d\sigma_{el}/d\Omega = 1.296 \times 10^{-15}/[E^2 \sin^4(\theta/2)]$ cm^2/sr.

For the inelastic electrons DCS from 5CC results [36] were utilized which, at energies of 37.5 eV, should be relatively unaffected by correction to the proper Coulomb phase [38,39]. "Density maps" (the cross section between ϑ and $\vartheta + d\vartheta$ divided by footprint area at ϑ) were made for the entire range of ϑ and for cases where the electrons were displaced stepwise in the interval $\{-0.5, 0.5$ mm$\}$

about the beam center. Then separately for both the 39.8-eV elastic and 33.5-eV inelastic electron cases the individual density maps were combined and integrated numerically to give density profiles as a function of position on the PSD. Due to the fact that only a limited number of trajectories were modeled on SIMION the curves show a jagged profile, but one which is close to what the detector should "see." In order to more accurately model the PSD signal, both the jagged elastic and inelastic profiles were smoothed using up to a tenth-order polynomial fitting routine. The results are shown in Fig. 4. The solid line represents the sum of the elastic and inelastic profiles and should reflect the net signal the PSD sees. The curves were integrated numerically over the position limits on the PSD to yield model number densities for the elastic, inelastic, and their summed scattering. Figure 4 represents a DCS-weighted sum of all trajectories along the 256-pixel (displacement x) direction. Trajectories which terminated at coordinates $y \neq 0$ were included and were projected onto the displacement direction. The total width in the y direction (12 pixels) was always much less than in the x direction (256 pixels).

The sensitivity of the elastic subtraction to the choice of x_{start}, x_{stop}, and n_{min} was assessed. Again referring to Fig. 4, if (ordinate) x_{start} is chosen to be 2.7", x_{stop} to be 3.55" and $n_{min} = 6.5$, then the integrated number density (area under the solid line) is 10.93 relative units. This may be compared with the "known" inelastic number density (the area under the short-dashed curve with no discrimination limits) of 9.91 relative units, for a discrimination error of 9.3%.

This type of modeling analysis was also carried out on the discrete ("jagged") set of curves resulting in a discrimination error of about 6%. For example, if $x_{start} = 2.6"$, $x_{stop} = 3.6"$, and $n_{min} = 6$, then the integrated number density measured 10.71 relative units and a discrimination error measured 7.5%; for $x_{start} = 2.7"$, $x_{stop} = 3.4"$, and $n_{min} = 1$ the integrated number density measured 10.08 relative units, for a discrimination error
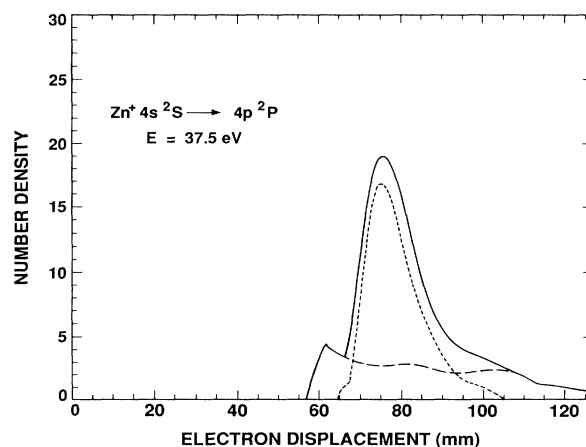

FIG. 4. Calculated "footprints" on the PSD for the case of elastic (———) and inelastic (- - -) scattering, and their sum (——) in Zn^+. The PSD extends between 69.9 and 108 mm.

of 1.7%. Because the unsmoothed curves are narrower than the smoothed curves (Fig. 4) the discrimination error from the former was calculated to be less than that in Fig. 4.

The actual uncertainties (see Table VII) are deduced from corresponding variations of x_{start}, x_{stop}, and n_{min} in the experimental data. This uncertainty in the elastic subtraction was found to be comparable to the discrimination errors above.

B. Method II: Footprint analysis for Mg^+

One may use a slightly different, and more preferable, method of elastic subtraction from the PSD image. In method II one tracks the amount of elastic scattering subtracted with successive increments of the baseline. The best choice is that at which one has subtracted off the total expected elastic-scattering signal, and no more. The elastic-scattering signal on the PSD is calculated from the Coulomb formula, and the fraction of the elastic scattering intercepted within the ROI of the PSD. In order to make the following discussion more concrete, shown in Fig. 5 are two sets of Mg^+ *experimental* data. One set is close to threshold ($E = 6.1$ eV) and the other at 26.8 eV (six times threshold). Each illustrates the reduction of the Coulomb scattering by use of the retarding voltages ("high" and "low") on grid G_2.

In the modeling, the angular extent of the elastically scattered electrons can generally be larger than the angular extent intercepted by the ROI set on the PSD. One defines two interception fractions F_A and F_B as

FIG. 5. Experimental inelastic (I) and elastic (E) scattering footprints for Mg^+ scattering at the indicated energies and retardation modes using grid G_2. Voltages on G_2 for LR are 0.0 V; voltages for HR are 26.0 ($E = 26.8$ eV) and 2.9 V ($E = 6.1$ eV).

$$F_A = \frac{[\text{elastic signal on PSD (ROI) in } \{\theta_c, \theta_m\}]}{(\text{total elastic signal in } \{\theta_c, \theta_m\})} ,$$

(12a)

$$F_B = \frac{[\text{elastic signal on PSD (ROI) in } \{0, \theta_c\}]}{(\text{total elastic signal in } \{0, \theta_c\})} ,$$

(12b)

where θ_m is the c.m. angle corresponding to $\vartheta = 90°$ scattering in the laboratory frame. The general trends of these interception fractions, as can be calculated from Eq. (11) over the appropriate range of θ, is that F_A is approximately 0.3–0.5 near threshold, and increases to ~ 0.8 at six times threshold (the dispersion of elastic scattering becomes smaller, and more of it strikes the PSD). The fraction F_B is zero at threshold (there is a large residual energy difference between the elastically and inelastically scattered electrons, and the ROI can be used to discriminate spatially against the former), ~ 0.6 at six times threshold, and approaches unity at approximately nine times threshold (the percentage difference between the elastically and inelastically scattered electron energies is smallest). It is also convenient to define partial integral elastic cross sections,

$$I_1 = \int_{\theta_c}^{\theta_m} \left[\frac{d\sigma_{el}}{d\Omega} \right] d\Omega ,$$

(13a)

$$I_2 = \int_0^{\theta_c} \left[\frac{d\sigma_{el}}{d\Omega} \right] d\Omega ,$$

(13b)

which define the integrated elastic scattering cross section intercepted by the PSD with the retarding grids "low" ($I_1 + I_2$) and "high" (I_2).

The effect of incrementing the baseline δ_n of the stored data is to shift the zero of the number density (ordinate of Fig. 4) by $0, 1, 2, \ldots, n$ counts, or equivalently to subtract a constant number of counts $0, 1, 2, \ldots, n$ from each pixel that makes up the solid curve. The fraction of the attenuated elastic signal in the interval $\{\theta_c, \theta_m\}$ is denoted as $k_A(\delta_n)$, and that in the interval $\{0, \theta_c\}$ as $k_B(\delta_n)$. By definition of the attenuation fraction, $k_A(\delta_0) = 1.00$, $k_A(\delta_n) = 0.00$, $k_B(\delta_0) = 1.00$, and $k_B(\delta_n)$, if desired, may be calculated from the argument below.

The sequence of baseline subtraction coupled with use of the retarding grids is shown in Table II. With no baseline subtraction (δ_0) one observes incoming counts proportional to the cross sections along the first row, with net transmitted counts indicated in the "low-high retard" column. The quantity $\mathcal{N}_n$ accounts for production of a weak, low-level background from incomplete background subtraction, small sampling statistics, etc. It results in background counts less than 1% of the maximum, and is eliminated at the first level ($\delta_n = 1$) of baseline subtraction. Increasing the baseline level serves to reduce the elastic components and the noise ($\mathcal{N}_1 < \mathcal{N}_0$), but not the inelastically scattered signal, proportional to $\sigma(E)$, which is sitting atop the background.

After n levels of baseline subtraction, one has reduced the "low retard" (LR) count level by an amount propor-
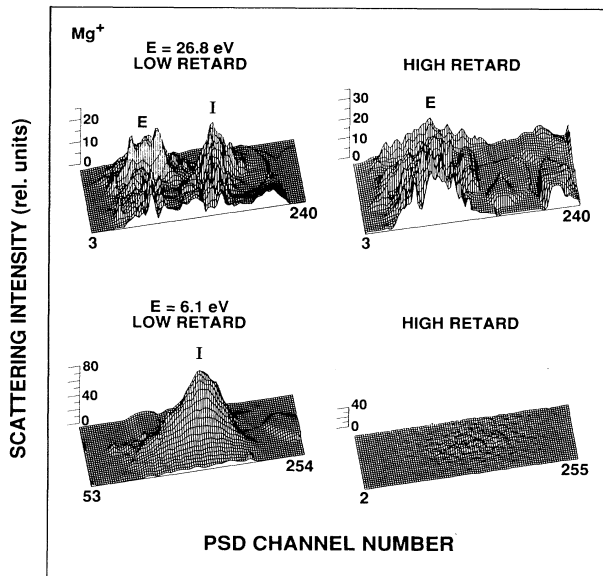
TABLE II. Variation of the sampled cross sections as a function of the baseline choice. The fractions F_A and F_B are defined in Eqs. (12a) and (12b) and the partial Coulomb integral cross sections I_1 and I_2 by Eqs. (13a) and (13b), respectively. See text for details.

| Baseline | Cross section | | |
	Low retard	High retard	Low-high retard
δ_0	$\sigma(E) + k_A(\delta_0)F_A I_1 + k_B(\delta_0)F_B I_2 + \mathcal{N}_0$	$k_B(\delta_0)F_B I_2 + \mathcal{N}_0$	$\sigma(E) + k_A(\delta_0)F_A I_1$
δ_1	$\sigma(E) + k_A(\delta_1)F_A I_1 + k_B(\delta_1)F_B I_2 + \mathcal{N}_1$	$k_B(\delta_1)F_B I_2 + \mathcal{N}_1$	$\sigma(E) + k_A(\delta_1)F_A I_1$
$\vdots$	$\vdots$	$\vdots$	$\vdots$
δ_n	$\sigma(E) + k_B(\delta_n)F_B I_2$	$k_B(\delta_n)F_B I_2$	$\sigma(E)$

tional to

$$\Delta_{LR}^{0,n} = F_A I_1 + [1 - k_B(\delta_n)]F_B I_2 + (\mathcal{N}_0 - \mathcal{N}_n) \quad (14a)$$

and the "high retard" (HR) to

$$\Delta_{HR}^{0,n} = [1 - k_B(\delta_n)]F_B I_2 + (\mathcal{N}_0 - \mathcal{N}_n) . \quad (14b)$$

The difference between Eqs. (14a) and (14b) is given by

$$\Delta_{LR}^{0,n} - \Delta_{HR}^{0,n} = F_A I_1 . \quad (14c)$$

The factor F_A on the right-hand side of Eq. (14c) is calculated from electron trajectories using the SIMION code in the present instrument geometry, and the factor I_1 is calculated from Eq. (13a). And hence, one has established a stopping point for the baseline subtraction: that at which an incremental baseline subtraction results in subtracted counts exceeding the Coulomb limit. This estimate of the Coulomb baseline should be consistent with the visual estimate from the experimental spectra.

To assess differences, method II was also applied to the Zn$^+$ case at 37.5 eV. The selected ROI was $2.6'' < x < 3.6''$. The baseline shift δ_n was varied from 0 to 5. For $\delta_n = 2.5$ (subtraction of 2.5 units from each pixel that makes up the solid line in Fig. 4) the integrated number density over all pixels yield 10.00 relative units, and compares favorably with the "known" inelastic number density (again, the area under the short-dashed curve with no discrimination limits) of 9.91 relative units, for a discrimination error of 0.9%. For a $\delta_n = 2$ subtraction the modeled number density is 10.69 relative units with a 7.3% discrimination error. A value of $\delta_n = 2.5$ corresponds at the 1% level to a baseline subtraction of the Coulomb scattering contribution within the ROI.

In actual data-taking practice the voltages on G_2 corresponding to LR and HR are chosen as follows: near threshold LR is set to 0.0 V; at three times threshold and above, LR is set to ~ -1.0 V to reject low-energy background electrons, without eliminating any inelastically scattered electrons which may scatter in the laboratory range $\vartheta\{0,90°\}$. The voltage setting on G_2 at HR is determined at all energies by the right-hand side of Eq. (10) when calculated for $\theta = 0°$ (corresponding to the highest-energy inelastically scattered electron). This setting also determines the value of ϑ_c. It can also be shown through Eqs. (10) and (13a) and comparisons with the measured inelastic cross sections that variations in the G_2 voltages of ± 0.2 eV (due to any uncertainties in contact potentials) have at most a 2% effect (occurring at thresh-

old) on the measured cross section. This source has been included in the 7% error estimate of the baseline subtraction (Table VII).

In a typical experiment the total number of counts over the PSD surface in a 500-sec run is (after beams chopping with its successive additions and subtractions) about 3000–60 000 counts over the 256×98 PSD array, with the maximum accumulated counts being about 200/pixel. The value of n_{min} is about 10/pixel. The elastic signal is usually about the same order of magnitude as the random scatter of background counts over the ROI, i.e., about 5–10/pixel.

As in method I, a footprint simulation was carried out for a test case of electrons scattered from Mg$^+$ at a c.m. energy of 15.0 eV ($E_e = 17.4$ eV). The retarding grids here limit the elastically scattered electrons to those which scatter through angles ϑ less than 30.2°. Basically the same type of trajectory analysis was carried out as for Zn$^+$: the SIMION code was used to launch both inelastically and elastically scattered electrons. The launch positions were varied in 0.25-mm steps over the interval $\{-0.5, 0.5 \text{ mm}\}$ about the beam center. A total of 360 trajectories (or 600 with interpolations) were computed to include forbidden transitions (see below).

Examples of the DCS used to construct the density maps are shown in Fig. 6 at two energies (15.0 and 26.8 eV) where the elastic-inelastic overlaps were greatest. The elastic DCS's [Eq. (11)] are shown at angles θ_c $\{32.5°, 180°\}$ at 15.0 eV, and $\{23.7°, 180°\}$ at 26.8 eV; the inelastic DCS's are taken from the present five-state close-coupling (5CC) Hartree-Fock (HF) calculations at 15.0 eV and the 5CC theory [36] at 26.8 eV. The elastic DCS's in Fig. 6 have their θ origin shifted by an amount equal to θ_c, since only elastic scattering through angles $\theta \geq \theta_c$ may interfere. Moreover, only the fraction F_A of the elastic scattering from θ_c to θ_m actually strikes the PSD [Eqs. (12a) and (12b)], and hence the elastic overlap in the ROI is even further mitigated. The correct comparison is between the inelastic DCS and $F_A \times$(elastic DCS), where F_A is in the range 0.3–0.8.

As a further refinement, included was an estimated contribution from two higher-energy levels, the $4s\,^2S$ at 8.655 eV and the $3d\,^2D$ at 8.864 eV. As pointed out by Henry [40], estimates of the collision strengths $\Omega(3s, 4s)$ and $\Omega(3s, 3d)$ from a unitarized Coulomb-Born approximation [41] were determined to be 15–20% that of $\Omega(3s, 3p)$ at energies less than 22 eV. A three-state close-coupling calculation [42] gives approximately the
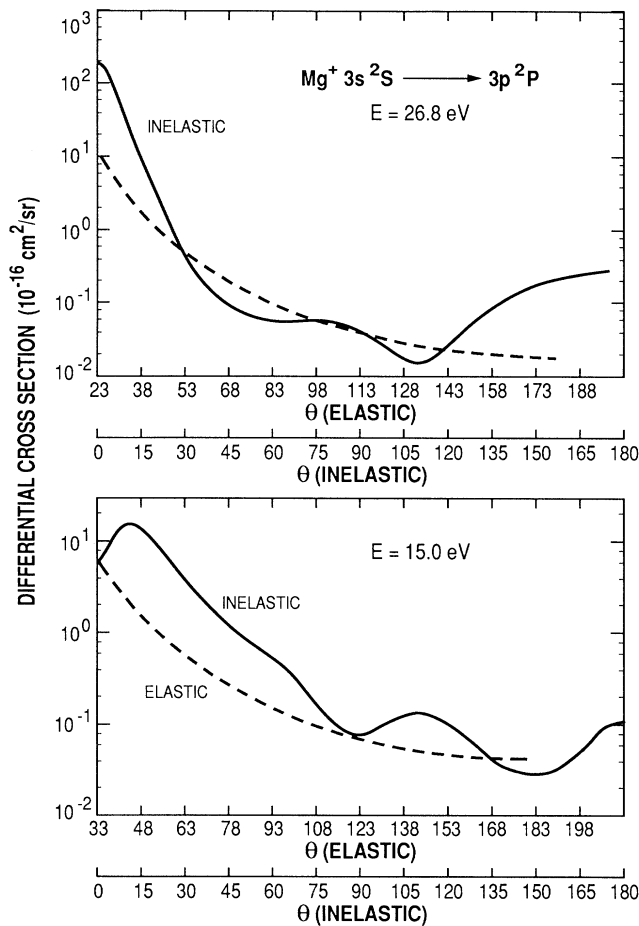
FIG. 6. Differential elastic and inelastic $4s \rightarrow 4p$ scattering cross sections for Mg^+ at energies of 26.8 (top) and 15.0 eV (bottom). Elastic DCS's in the interval $\{\theta_c, \theta_m\}$ are from Eq. (11), and inelastic DCS's are from 5CC (HF) at 15.0 eV (present work) and from Ref. [36] at 26.8 eV.

$E = 7.6$ eV (in order to obtain approximately the same threshold energy units at 15 eV for the forbidden transitions). Some justification for this exists in the similarity of the angular distributions for these forbidden and allowed transitions found in crossed-beam results at $E = 50$ eV [9]. Results for the individual contributions and a net total footprint are shown in Fig. 7. In analyzing this footprint an allowed spread of $2.4'' < x < 4.1''$ (as well as other ranges of x not listed here) was used, and the baseline shift δ_n was varied from zero to four relative units. The modeled $^2S \rightarrow ^2P$ number density (area under the short-dashed curve with no discrimination limits) measures 9.35. For $\delta_n = 2$ the integrated number density for the sum of inelastic, elastic, and forbidden contributions is 10.1 for a modeling error of 8.0%; for $\delta_n = 2.5$ the integrated number density is 9.45 for a modeling error of 1.1%; and for $\delta_n = 3$ the integrated number density is 8.86 for an error of -5.2%.

Based on the SIMION modeling, for a given value of δ_n one can estimate how much of the total signal was composed of the individual $(3s, 3p)$ allowed transition, the $(3s, 4s), (3s, 3d)$ forbidden transitions, and elastic scattering. These percentages are listed in Table III.

A simulation was also carried out of the experimental spectra shown in Fig. 5 at $E = 26.8$ eV under conditions of high and low retardation. The elastic and inelastic DCS's used are shown in Fig. 6 and the simulated spectra in Fig. 8. Contribution from the $^2S \rightarrow ^2D$ transition was considered negligible at these higher energies and was not included in the calculations. There is good qualitative agreement between the simulations and spectra. In particular, one sees a clear separation between the elastic and inelastic features and, underlying the inelastic feature, a tail of the elastic scattering which can be subtracted.

There are a number of limitations to methods I and II. First, the inelastic signal density/pixel should be appreciably larger in magnitude than the elastic signal
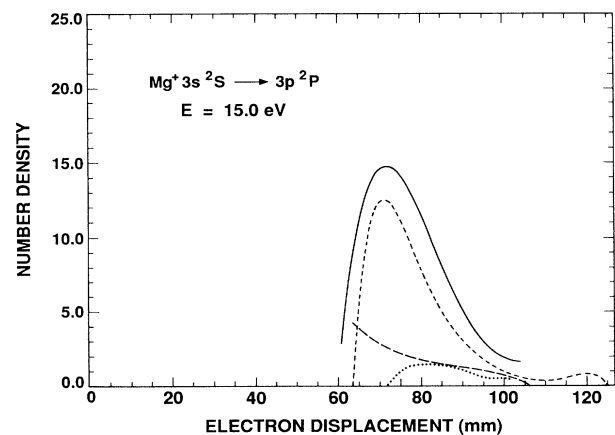
same percentage contribution for these forbidden transitions. Also, optical excitation measurement of Zapesochnyĭ *et al.* [43] and Kel'man [44] showed a small cascading contribution (less than 10–15%) from these higher levels to the $3p\ ^2P$ level, consistent with small values for $\Omega(3s, 4s)$ and $\Omega(3s, 3d)$. Thus, to estimate the forbidden contributions to the "footprint" the combined $(3s, 4s)$ and $(3s, 3d)$ collision strengths were conservatively assumed to be 15% of the collision strength of the $(3s, 3p)$ resonance transition. Finally, the actual $(3s, 4s)$ and $(3s, 3d)$ signals on the PSD also depend on (a) the DCS of these forbidden transitions and (b) the transverse dispersion by the analyzing plates of the electrons having excited them. These electrons have a residual energy ~ 4 eV less than that of electrons having excited the $3s\ ^2S \rightarrow 3p\ ^2P$ transition.

The required DCS's for the $(3s, 4s)$ and $(3s, 3d)$ transitions were not available. Hence their DCS's were modeled by scaling the DCS obtained from the present 5CC (HF) calculation for the $^2S \rightarrow ^2P$ transition at

FIG. 7. Calculated "footprints" on the PSD for the case of elastic scattering (————), inelastic ^2P scattering (- - -), inelastic ^2S and $^2D(\cdot \ \cdot \ \cdot \ \cdot)$ scattering and their sum (————) in Mg^+. The PSD extends between 69.9 and 108 mm.

TABLE III. Percentage contributions from trajectory modeling of the allowed, forbidden, and elastic transitions to the Mg^+ footprint for various values of the baseline shift δ_n.

δ_n	Allowed $(3s,3p)$ $(\%)$	Forbidden $(3s,4s),(3s,3d)$ $(\%)$	Elastic $(\%)$
		Contribution	
0	70.7	5.85	23.4
0.25	72.9	6.00	21.1
0.5	75.2	4.60	20.2
1.0	80.3	1.52	18.2
1.5	86.1	0.06	13.8
2.0	92.8		7.21
2.5	98.9		1.10

density/pixel within the x_{start} and x_{stop} discriminator settings. This suggests that a typical oscillator strength of $f \geq 0.2$ is required (for Zn^+ $f = 0.732$, and for Mg^+ $f = 0.940$). Also, the inelastic differential cross section must be forward peaked at energies away from threshold. One also requires the grids to be used to subtract off the electrons which elastically scatter through angles less than ϑ_c as calculated from Eq. (10) with $\Delta E_{c.m.} = 6.011$ eV. Note that a large fraction of electrons elastically scattered through angles $\vartheta > \vartheta_c$ do not strike the viewing area of the PSD due to dispersion by AP. Observed experimental errors due to various choices of baseline and counting statistics do not exceed 7%. This is supported by typical experimental variations found between two measurements at the same energy and is consistent with estimates of error from the modeling.
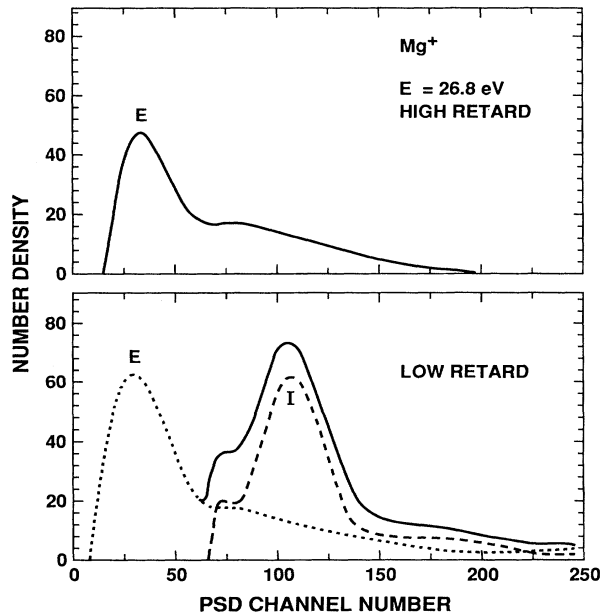
FIG. 8. Calculated "footprints" on the PSD for elastic scattering $(E, \cdots)$ and inelastic ${}^2P$ scattering $(I, - - -)$ and their sum (———) in Mg^+. Shown are simulations of the experimental spectra at $E = 26.8$ eV (Fig. 5) for the cases of "high retard" and "low retard."

The footprint modeling was carried out at a number of energies in Zn^+ (7.0 and 37.5 eV), Mg^+ (5.0, 15.0, 26.8, and 35.9 eV), and O^+ (17.0 eV, not reported here). The experience gained shows that there are generally three regions of electron energy to consider: (i) At threshold, there is little spatial overlap between the inelastic and elastic signals due to their separation by the plates AP. Moreover, the inelastic signal is largest here. (ii) At the highest energies, between about five and nine times threshold, the inelastic DCS is forward peaked, and the plates still have sufficient dispersion to separate the elastic (at angles $\vartheta < \vartheta_c$) and inelastic signals. At about ten times threshold and higher the inelastic signal weakens and is difficult to extract from the elastic signal due to the decreased spatial separation by the plates. (iii) In an intermediate-energy region, about three times threshold, two competing factors are present. The inelastic DCS is still somewhat isotropic, and the elastic scattering cross section (varying as E_e^{-2}) competes, as seen for just this case in Fig. 6. In all three regions one would still require some minimum excitation cross section, roughly corresponding to $f \geq 0.2$.

By way of example, consider an electron having 9.99-eV (lab) energy which is scattered in the forward direction ($\vartheta = 0°$) and left with 5.00 eV (lab) after having excited the 4.42-eV resonance transition. Prior to data taking, (a) the SIMION code is first used to calculate the required analyzing-plate voltage needed to deflect the 5.00-eV electron beam to the center of the ROI of the PSD. (b) Then, a 5.00-eV beam of very low current ($\sim 10^{-14}$ A) is directed onto the PSD to check the calculated plate voltage. The shape of the beam on the PSD can be seen as a slightly elongated, elliptical spot. (c) Following that, an actual data run is carried out. The cathode (electron-gun) energy is raised to 9.99 eV to give 5.00-eV residual electron energy, and merged with the ion beams. (d) A beams profile is measured. (e) With the retarding grid G_2 set to 0.0 V (LR mode), data accumulation is started for 500 sec, with both beams modulated. In this mode both elastically and inelastically scattered electrons in the angular range $\{0, 90°\}$ (lab) are transmitted. (f) A second data run is then carried out with G_2 set to -5.10 eV (HR mode). In this mode all inelastically scattered electrons and elastically scattered electrons in the range $\{\vartheta_c, 90°\}$ are repelled. Elastically scattered electrons in the range $\{0, \vartheta_c\}$ are transmitted. (g) A second beams profile is

TABLE IV. Theoretical and experimental [50] binding energies (in atomic units) for the low-lying states of Mg$^+$.

Level	5CC (HF)	5CC (HF)+V_{pol}	5CC (CI)	Experimental
		Binding energy		
$3s$	$-0.541\,438$	$-0.552\,541$	$-0.552\,54$	$-0.552\,54$
$3p$	$-0.384\,160$	$-0.389\,740$	$-0.390\,49$	$-0.389\,74$
$3d$	$-0.224\,906$	$-0.226\,802$	$-0.238\,77$	$-0.226\,80$
$4s$	$-0.231\,699$	$-0.234\,356$	$-0.231\,78$	$-0.234\,48$
$4p$	$-0.183\,411$	$-0.185\,034$	$-0.189\,67$	$-0.185\,16$

measured after the data accumulation. (h) After computer subtraction of the two data sets one can clearly see the footprint of the inelastic signal on the PSD. In fact, close to threshold, where the inelastic cross section is largest, and the elastic-inelastic spatial separation is greatest, one can see the footprint without subtraction. The ROI is quite well defined, and has a roughly elliptical shape of 50×100 pixels (the total detector area is 96×256 pixels), with about 4–20 counts/pixel. The remainder of the PSD has a low-intensity noise level, and some outer-lying elastic-scattering signal, of about 0–3 counts/pixel. The specific area of inelastic footprint is then marked off by an ROI ($x_{start}, x_{stop}, y_{start}, y_{stop}$) by the operator. The total counts within this ROI may be calculated, and the baseline value adjusted between 0–10 counts/pixel to subtract off the elastically scattered signal and random noise.

III. THEORETICAL CONSIDERATIONS

Two sets of five-state close-coupling calculations (5CC) were carried out of the $e-$Mg$^+$ scattering. The main differences in the calculations lay in the use of a Hartree-Fock (HF) or configuration-interaction (CI) approach to the calculation of the target wave function and in the method of calculation of the scattering partial waves. The two approaches are designated as 5CC (HF) and 5CC (CI).

A. Calculations in the 5CC (HF) approach

The underlying approach and methodology of the calculation is similar to those undertaken recently in a series of studies on electron-alkali ion scattering [45,46]. The target states ($3s$, $3p$, $4s$, $3d$ and $4p$) are constructed by adding a semiempirical polarization potential to a Hartree-Fock (HF) calculation. Briefly, the HF wave function for the Mg$^+$ $3s$ ground state is first obtained. The wave function for the core orbitals ($1s$, $2s$, and $2p$) is then frozen and a polarization potential of the form [47]

$$V_{pol}(r) = \frac{-\alpha_d}{2r^4}[1-\exp(-r^6/\rho_l^6)] \tag{15}$$

is added to the Hamiltonian and used in the calculation of the wave function for the valence orbitals. The value chosen for the static dipole polarizability (α_d) was $0.4814a_0^2$. This was taken from a large-basis configuration-interaction calculation [48,49]. The values of ρ_l were adjusted until theoretical and empirical binding energies for the $3s$, $3p$, and $3d$ levels were in agreement (see Table IV). The values for ρ_l were $\rho_0 = 1.1222a_0$, $\rho_1 = 1.228a_0$, $\rho_2 = 1.40a_0$, and for ρ_3 and all higher values of l ρ_l was fixed at $1.48a_0$. It has been demonstrated in previous works that besides giving more-accurate energy levels, this adjustment method for the ρ_l values gives more-accurate oscillator strengths and cross sections. The oscillator strengths for the present wave functions are listed in Table V. When computing the oscillator strengths, a modified form of the dipole matrix element was used [45,46].

The close-coupling calculations were performed with a modified version of the RMATRX program [52] and included all five states. The Hamiltonian used for the calculation of the K matrix was modified by the inclusion of the one-body polarization potential and the two-body dielectronic polarization potential.

TABLE V. Comparison of the oscillator strengths used in the present work with those of a large basis multiconfiguration Hartree-Fock (MCHF) calculation [51].

Transition	5CC (HF)+V_{pol}	f_L	f_V	MCHF
		Oscillator strength		
		5CC (CI)		
$3d$-$3p$	0.913	0.94	0.92	0.913
$3s$-$4p$	0.000\,88	0.0004	0.0003	0.000\,97
$3p$-$4s$	0.150	0.15	0.15	0.150
$3p$-$3d$	0.942	0.97	0.83	
$4s$-$4p$	1.393	1.41	1.45	1.394
$3d$-$4p$	0.171	0.17	0.19	

Partial waves for $l=0-11$ were computed with the RMATRX program. Higher partial waves were obtained within the unitarized Coulomb-Born approximation (UCBA). Naturally, the polarization potentials were included in the scattering Hamiltonian for the UCBA calculation. The total number of partial waves required to obtain a converged differential cross section varied from 20 at 5 eV, to 36 at 7.5 eV, to 70 at 15 eV.

B. Calculations in the 5CC (CI) approach

Here, the 1s, 2s, 2p, and 3s radial functions were those of the $2p\,^63s\,^2S$ ground state given by Clementi and Roetti [53]. The 3p and 3d radial functions were optimized on $2p\,^63p\,^2P^o$ and $2p\,^63d\,^2D$ states, respectively, while the orbitals 4s and 4p were chosen to improve the energies of the $2p\,^64s\,^2S$ and $2p\,^64p\,^2P^o$ states, respectively. The additional orbitals 4d and 4f were optimized on the ground $2p\,^63s\,^2S$ state. The radial part of each orbital was represented as a sum of Slater-type functions

$$P_{nl}(r) = \sum_{i=1}^{k} c_i r^{p_i} \exp(-\xi_i r) \ . \tag{16}$$

The parameters of the radial functions 3p, 3d, 4s, 4p, 4d, and 4f are listed in Table VI. In the case of 4s, 4p, 4d, and 4f orbitals, $k=n-l$ were chosen so that the coefficients c_i were uniquely specified by the orthogonality conditions on P_{nl}.

A large number of configurations were considered to represent the lowest five states of Mg^+ that were includ-

ed in the close-coupling expansion. In order to construct these configurations, up to three-electron excitations were considered by opening 2s and 2p subshells. In the final calculation, all configurations with smaller weights (<0.004) were dropped and a total of 27 configurations were retained. The calculated binding energies for the five states are given in Table IV, where there are compared with the present experiment and the 5CC (HF) calculation. The absorption oscillator strengths in length (f_L) and velocity (f_V) formulations for the dipole-allowed transitions obtained using configuration-interaction wave functions are listed in Table V. The good agreement between length and velocity formulations and other calculations provides confidence in the accuracy of the wave functions. The oscillator strength for the 3s-4p transition is small since there are cancellation effects.

The excitation cross sections for the resonance 3s-3p transition were calculated at 4.5, 6, 8, 10, 20, and 30 eV using the R-matrix method [52]. At each electron energy, cross sections for lower angular momenta ($l=0-9$) were calculated with exchange and correlation terms included, while for higher angular momenta ($l>9$) a close-coupling approximation with no exchange and correlation terms was used.

IV. RESULTS AND DISCUSSION

Present experimental and theoretical electron excitation cross sections for the $3s\,^2S \to 3p\,^2P$ transition in Mg^+ are shown in Fig. 9. Experimental uncertainties at the 1σ and 1.7σ (total error) confidence level of random

TABLE VI. Values of parameters of the radial functions for Mg^+ in the 5CC (CI) method.

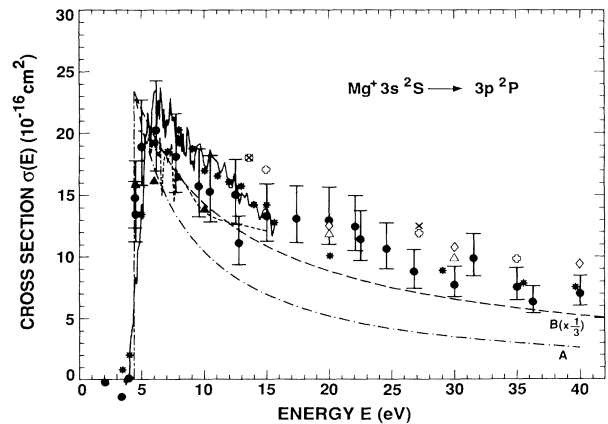| Orbital	c_i	p_i	ξ_i
3p	−0.136 64	2	3.339 55
	−0.052 23	2	6.452 17
	−0.096 31	3	2.065 24
	0.189 87	3	1.641 40
	0.918 60	3	0.969 11
3d	0.029 68	3	2.368 16
	−1.641 27	3	1.781 75
	8.788 74	3	1.306 99
	20.695 48	3	1.017 94
	−27.151 27	3	1.089 79
4s		1	9.974 00
		2	3.840 21
		3	1.235 54
		4	0.736 53
4p		2	4.306 57
		3	0.884 40
		4	0.640 07
4d		3	2.801 09
		4	0.860 83
4f		4	2.802 34

FIG. 9. Experimental and theoretical excitation cross sections for the $3s\,^2S \to 3p\,^2P$ (h,k) transitions in Mg^+. Symbols are as follows: ($\bullet$) present measurements, ($*$) photon-emission measurements of Zapesochnyĭ et al. [43], (———) photon-emission measurements of Zapesochnyĭ et al. [54], ($\bigcirc$) distorted-wave calculation of Pangantiwar and Srivastava [57], ($\times$) distorted-wave, polarized-orbital calculation of Kennedy, Meyerscough, and McDowell [58], ($\lozenge$) 5CC calculation of Msezane and Henry [55], (---) present 5CC (HF) calculations, and ($\blacktriangle$) present 5CC (CI) calculations. Gaunt-factor results are taken from Refs. [59] (A) and [60] (B).

error are listed in Table VII, and cross-section values are listed in Table VIII. With the use of a single PSD in the forward direction, or with relatively low ion velocities, one measures only the forward ($0°-90°$, laboratory frame) portion of the differential electron scattering cross section. While for an optically allowed transition this represents the major part of the integral cross section [10], an estimate is nevertheless required for the $90°-180°$ contribution, especially in the threshold region where the DCS is relatively more isotropic. The backward-scattered cross section was obtained from the present 5CC (HF) and 5CC (CI) calculations such as those shown in Fig. 6, and served to raise the cross section by the factors listed in Table VIII, column 3.

Basically, one has three sets of experimental results: the present (without cascade), and the works of Zapeso-chnyĭ *et al.* [43,54] (with cascade). One also has six sets of theoretical or semiempirical calculations: a 5CC calculation of Msezane and Henry [55], present 5CC calculations, a 4CC calculation [56], a distorted-wave calculation of Pangantiwar and Srivastava [57], a distorted-wave, polarized-orbital calculation of Kennedy, Meyer-scough, and McDowell [58], and the semiempirical

TABLE VII. Experimental uncertainties. The total quadrature errors correspond to 1.7σ or a 90% confidence limit.

Source of uncertainty	Uncertainty at the 1σ confidence level (%)
Counting statistics	1.0
Form factor	6.0
Path length	1.0
Electron-current measurement	0.5
Ion-current measurement	0.5
PSD efficiency calibration	2.0
Choice of baseline and pixel area	7.0
Dead-time correction[a]	$+2.0$
	-0.0
Forward-to-back correction (near threshold)	5.0
Total quadrature error	
Near threshold	$+21\%$
	-18%
Above threshold	$+20\%$
	-16%

[a]This one-sided uncertainty is added linearly to the quadrature combination of the remaining uncertainties.

TABLE VIII. Present experimental and theoretical results for the $3s\,{}^2S \rightarrow 3p\,{}^2P$ transition in Mg^+. Uncertainty in the experimental data is given at the 90% (1.7σ) confidence limit of random error. Uncertainty in the energy E is 0.1 eV.

Energy E (eV)	Maximum c.m. angle(deg)[a]	Forward-to-back correction[b]	Cross section $\sigma(E)$ (10^{-16} cm^2)		
			Expt.	5CC (HF)	5CC (CI)
3.96	180.0		0.07	0.00	0.00
4.47	180.0		14.8		
4.50	180.0		13.4		15.9
5.00	113.2	1.210	18.9	20.2	
6.00				18.9	16.2
6.14	103.2	1.216	20.2		
7.73	99.5	1.190	18.1		
8.00					16.5
9.57	97.6	1.086	15.7		
10.0				13.2	13.9
10.5	97.0	1.070	15.2		
12.5	96.1	1.060	15.0		
12.8	96.0	1.058	11.1		
15.0	95.3	1.047	13.3	12.1	
17.4	94.8	1.043	13.1		
20.0	94.4	1.031	13.0		11.9
22.1	94.1	1.022	12.4		
22.5	94.1	1.020	11.4		
24.6	93.9	1.010	10.6		
26.8	93.7	1.001	8.76		
30.0	93.4		7.69		9.90
31.5	93.3		9.84		
35.0	93.1		7.50		
36.3	93.1		6.29		
40.0	92.9		7.00		

[a]Assuming $\vartheta = 90°$ collection in the laboratory frame.
[b]From an average of 5CC (HF) and 5CC (CI) results, or 5CC (CI) results alone. Where used, the 5CC (HF) resonance structure was averaged over a 350-meV electron energy width (FWHM).

TABLE IX. Experimental results for the $4s\,^2S \rightarrow 4p\,^2P$ transition in Zn^+, tabulated from Ref. [11]. Uncertainty in the experimental data is given at the 90% (1.7σ) confidence level of random error. Uncertainty in the energy E is 0.1 eV.

Energy E (eV)	Maximum c.m. angle (deg)[a]	Forward-to-back correction[b]	Experimental cross section $\sigma(E)$ $(10^{-16}\ cm^2)$
6.01	180.0		4.94
6.46	105.9	1.676	12.0
7.87	97.9	1.308	8.91
10.2	95.1	1.236	6.95
12.6	94.1	1.129	6.77
14.0	93.6	1.082	5.36
16.5	93.3	1.043	4.45
19.0	92.9	1.026	4.82
24.0	92.5		4.03
27.0	92.3		3.55
30.0	92.2		3.90
32.6	92.0		2.91
36.7	91.8		2.63

[a]Assuming $\vartheta = 90°$ collection in the laboratory frame.
[b]From 15CC theoretical results of Ref. [63], averaged over their resonance structure.

Gaunt-factor expression as given in Refs. [59] (curve A) and [60] (curve B). These last results were calculated from the relation

$$\sigma(U) = \frac{8\pi^2 a_0^2}{\sqrt{3}} \left[\frac{E_H}{\Delta E}\right]^2 f_{ij} g(U) U^{-1} , \qquad (17)$$

where a_0 is the Bohr radius, E_H the Rydberg energy (13.61 eV), ΔE the transition energy between states i and j, and f_{ij} the corresponding oscillator strength. The quantity U is the incident electron energy in threshold units $(U = E/\Delta E)$, and $g(U)$ is a semiempirical factor. For $g(U)$ van Regemorter [59] suggests a constant value $\bar{g} = 0.2$, while Mewe [60] suggests a form

$$g(U) = A + BU^{-1} + CU^{-2} + D \ln U , \qquad (18)$$

where $A = 0.6$, $B = C = 0$, and $D = 0.28$ for an allowed transition with no change is principal quantum number. An oscillator strength for Mg^+ of $f = 0.940$ was used [61].

Experimental and theoretical results for Mg^+ are compared in Fig. 9. Experimental uncertainties are listed in Table VII, and values for integral cross sections in Mg^+ and Zn^+ are listed in Tables VIII and IX, respectively. The Zn^+ integral cross sections listed in Table IX are from Ref. [11] and are tabulated herein for convenience. Each data point in Fig. 9 is a result of averaging two-four measurements together. The resonance structure is predicted in the present calculations. It is also predicted and seen in Ref. [53], and it was first calculated by Burke and Moores [62]. One finds good agreement of the present data with theories in Refs. [55,57,58] and with the present 5CC (HF) and 5CC (CI) theories. The semiempirical Gaunt-factor result of Ref. [59] gives a reasonable cross section at threshold, but one that decreases to about half the experimental value above threshold. Results of Ref. [60] give a cross section which is about a factor of 3 too large. Such differences in astrophysical use of collision strengths can lead to orders-of-magnitude errors in calculations of solar-stellar plasma electron temperatures and densities.

Agreement of the present data with results of Zapesochnyǐ et al. near threshold, where cascading is absent, is within combined experimental errors. One might have expected photon-emission data lying above the $4s\,^2S$ energy (8.66 eV) to have a cascade contribution, and hence to lie above the present data. For Mg^+ this cascading appears to be a small effect, but a better assessment must await an accurate cascade calculation.

ACKNOWLEDGMENTS

[1] See, for example, R. A. Phaneuf, in *Atomic Processes in Electron-Ion and Ion-Ion Collisions,* edited by F. Brouillard (Plenum, New York, 1986); A. Chutjian, High Temp. Sci. **17,** 135 (1984).

[2] G. A. Doschek and A. Bhatia, Astrophys. J. **358,** 338 (1990).

[3] J. C. Raymond and A. K. Dupree, Astrophys. J. **222,** 379 (1978).

[4] C. Martin and S. Bowyer, Astrophys. J. **350,** 242 (1990).

[5] D. E. Shemansky, J. Geophys. Res. **92,** 6141 (1987).

[6] D. E. Post, in *Physics of Ion-Ion and Electron-Ion Collisions,* edited by F. Brouillard and J. Wm. McGowan (Plenum, New York, 1983), p. 37.

[7] E. P. Wigner, Phys. Rev. **73,** 1002 (1948).

[8] A. Chutjian and W. R. Newell, Phys. Rev. A **26,** 2271 (1982); A. Chutjian, A. Z. Msezane, and R. J. W. Henry, Phys. Rev. Lett. **50,** 1357 (1983).

[9] I. D. Williams, A. Chutjian, and R. J. Mawhorter, J. Phys. B **19,** 2189 (1986).

[10] I. D. Williams, A. Chutjian, A. Z. Msezane, and R. J. W. Henry, Astrophys. J. **299,** 1063 (1985).

[11] S. J. Smith, K-F. Man, R. J. Mawhorter, I. D. Williams, and A. Chutjian, Phys. Rev. Lett. **67,** 30 (1991); in *Atomic Physics 12,* edited by Jens C. Zorn and Robert R. Lewis, AIP Conf. Proc. No. 233 (AIP, New York, 1991).

[12] E. K. Wåhlin, J. S. Thompson, G. H. Dunn, R. A. Phaneuf, D. C. Gregory, and A. C. H. Smith, Phys. Rev. Lett. **66,** 157 (1991).

[13] A preliminary account of this work was given at the XVII International Conference on Physics of Electron-Atom Collisions, Brisbane, ACT, 1991. See *Book of Abstracts,* edited by I. E. McCarthy, W. R. MacGillivray, and M. C. Standage (Griffith University, Nathan, Australia, 1991), p. 279.

[14] L. Wåhlin, Nucl. Instrum. Methods **27,** 55 (1964); M. Menzinger and L. Wåhlin, Rev. Sci. Instrum. **40,** 102 (1968).

[15] D. Auerbach, R. Čaćak, R. Caudano, T. D. Gaily, C. J. Keyser, J. Wm. McGowan, J. B. A. Mitchell, and S. F. J. Wilk, J. Phys. B **10,** 3797 (1977).

[16] See, for example, A. Chutjian, Rev. Sci. Instrum. **50,** 347 (1979); K. Jung, Th. Antoni, R. Muller, K-H. Kochem, and H. Ehrhardt, J. Phys. B **15,** 3535 (1982); S. Trajmar and D. F. Register, in *Electron-Molecule Collisions,* edited by I. Shimamura and K. Takayanagi (Plenum, New York, 1984).

[17] F. Brouillard and W. Claeys, in *Physics of Ion-Ion and Electron-ion Collisions* (Ref. [6]), p. 415.

[18] H. S. W. Massey and E. H. S. Burhop, *Electronic and Ionic Impact Phenomena* (Oxford University, London, 1969), Vol. 1.

[19] M. T. Bernius, K-F. Man, and A. Chutjian, Rev. Sci. Instrum. **59,** 2418 (1988).

[20] K. T. Dolder and B. Peart, Rep. Prog. Phys. **39,** 693 (1976).

[21] P. Cloutier and L. Sanche, Rev. Sci. Instrum. **60,** 1054 (1989); L. Sanche (private communication).

[22] A. Stamatović and G. J. Schulz, Rev. Sci. Instrum. **39,** 1752 (1968); **41,** 423 (1970).

[23] M. R. McMillan and J. H. Moore, Rev. Sci. Instrum. **51,** 944 (1980).

[24] D. Roy, Rev. Sci. Instrum. **43,** 535 (1972).

[25] By using cylindrical plates, one may compensate for this shear by having the faster electrons travel a longer dis-

tance. See S. M. Hutchins, P. G. Coleman, R. J. Stone, and R. N. West, J. Phys. E **19,** 282 (1986).

[26] D. A. Dahl and J. E. Delmore, Idaho National Engineering Laboratory Report No. EGG-CS-7233 Rev. 2, 1988 (unpublished).

[27] D. E. Nitz, M. W. Geis, K. A. Smith, and R. D. Rundel, Rev. Sci. Instrum. **47,** 306 (1976).

[28] L. Molyneux, K. T. Dolder, and B. Peart, J. Phys. E **4,** 149 (1971); K. T. Dolder, in *Case Studies in Atomic Collision Physics,* edited by E. W. McDaniel and M. R. C. McDowell (North-Holland, Amsterdam, 1969), Vol. I, Chap. 5.

[29] C. C. Havener, M. S. Huq, H. F. Krause, P. A. Schulz, and R. A. Phaneuf, Phys. Rev. A **39,** 1725 (1989).

[30] *Handbook of Chemistry and Physics,* 70th ed. (CRC, Boca Raton, FL, 1989), pp. E-93 and E-94.

[31] R. S. Gao, P. S. Gibner, J. H. Newman, K. A. Smith, and R. F. Stebbings, Rev. Sci. Instrum. **55,** 1756 (1984).

[32] A. Müller, N. Djurić, G. H. Dunn, and D. S. Belić, Rev. Sci. Instrum. **57,** 349 (1986).

[33] Secondary electron emission coefficients of tungsten are summarized in Atomic Data for Controlled Fusion Research, Oak Ridge National Laboratory Report No. ORNL-5207, edited by C. F. Barnett, J. A. Ray, E. Ricci, M. I. Wilker, E. W. McDaniel, E. W. Thomas, and H. B. Gilbody (Oak Ridge National Laboratory, Oak Ridge, TN, 1977), Sec. D.2.12.

[34] W. R. Leo, *Techniques for Nuclear and Particle Physics Experiments* (Springer-Verlag, New York, 1987), p. 114; M. Lampton and J. Bixler, Rev. Sci. Instrum. **56,** 164 (1985).

[35] Quantar Technology, Inc., Santa Cruz, CA.

[36] A. Z. Msezane and R. J. W. Henry, Phys. Rev. A **25,** 692 (1982); and private communication.

[37] R. G. Newton, *Scattering Theory of Waves and Particles* (McGraw-Hill, New York, 1966), Sec. 14.6.

[38] J. Mitroy, J. Phys. B **21,** L25 (1988).

[39] J. Mitroy, Phys. Rev. A **37,** 649 (1988).

[40] R. J. W. Henry, Phys. Rep. **68,** 1 (1981).

[41] M. Blaha, Astron. Astrophys. **16,** 437 (1972).

[42] K. Bhadra and R. J. W. Henry, Bull. Am. Phys. Soc. **189,** 55 (1979).

[43] I. P. Zapesochnyĭ, V. A. Kel'man, A. I. Imre, A. I. Daschenko, and F. F. Danch, Zh. Eksp. Teor. Fiz. **69,** 1948 (1975) [Sov. Phys. JETP **42,** 989 (1975)].

[44] V. A. Kel'man, Sov. Phys. J. **8,** 1089 (1975).

[45] J. Mitroy and D. W. Norcross, Phys. Rev. A **39,** 537 (1989).

[46] J. Mitroy, D. C. Griffin, D. W. Norcross, and M. S. Pindzola, Phys. Rev. A **38,** 3339 (1988).

[47] D. W. Norcross and M. J. Seaton, J. Phys. B **9,** 2983 (1976).

[48] H. J. Werner and W. Meyer, Phys. Rev. A **14,** 915 (1976).

[49] W. Muller, J. Flesch, and W. Meyer, J. Chem. Phys. **80,** 3297 (1984).

[50] S. Bashkin and J. O. Stoner, *Atomic Energy Levels and Grotrian Diagrams* (North-Holland, Amsterdam, 1975), Vol. 2.

[51] C. Froese-Fischer, Can. J. Phys. **54,** 1465 (1976).

[52] K. Berrington, P. G. Burke, M. LeDourneuf, W. D. Robb, K. T. Taylor, and V. K. Lan, Comput. Phys. Commun. **14,** 367 (1978).

[53] E. Clementi and C. Roetti, At. Data Nucl. Data Tables **14,** 177 (1974).

[54] I. P. Zapesochnyĭ, A. I. Daschenko, V. I. Frontov, A. I. Imre, A. N. Gomonai, V. I. Lend'el, V. T. Navrotskiĭ, and E. P. Sabad, Pis'ma Zh. Eksp. Teor. Fiz. **39**, 45 (1984) [JETP Lett. **39**, 51 (1984)].

[55] A. Z. Msezane and R. J. W. Henry, Phys. Rev. A **33**, 1636 (1986).

[56] C. Mendoza, J. Phys. B **14**, 2465 (1981).

[57] A. W. Pangantiwar and R. Srivastava, J. Phys. B **21**, L219 (1988).

[58] J. V. Kennedy, V. P. Meyerscough, and M. R. C. McDowell, J. Phys. B **11**, 1303 (1978).

[59] H. van Regemorter, Astrophys. J. **126**, 906 (1962).

[60] R. Mewe, Astron. Astrophys. **20**, 215 (1972).

[61] W. L. Wiese, M. W. Smith, and B. M. Miles, *Atomic Transition Probabilities*, Natl. Stand. Ref. Data Ser., Natl. Bur. Stand. (U.S.) Circ. No. 22 (U.S. GPO, Washington, DC, 1969), Vol. II.

[62] P. G. Burke and D. L. Moores, J. Phys. B **1**, 575 (1968).

[63] M. S. Pindzola, N. R. Badnell, R. J. W. Henry, D. C. Griffin, and W. J. van Wyngaarden, Phys. Rev. A **44**, 5628 (1991).